The Astrophysical Journal, 843:18 (11pp), 2017 July 1 https://doi.org/10.3847/1538-4357/aa767d

Quasar Feedback in the Ultraluminous Infrared Galaxy F11119+3257: Connecting the Accretion Disk Wind with the Large-scale Molecular Outflow

S. Veilleux[1,2], A. Bolatto[1,2], F. Tombesi[3,4,5], M. Meléndez[1,6,7], E. Sturm[8], E. González-Alfonso[9], J. Fischer[10], and D. S. N. Rupke[11]
[1] Department of Astronomy, University of Maryland, College Park, MD 20742, USA; veilleux@astro.umd.edu
[2] Joint Space-Science Institute, University of Maryland, College Park, MD 20742, USA
[3] X-ray Astrophysics Laboratory, NASA Goddard Space Flight Center, Greenbelt, MD 20771, USA
[4] Department of Astronomy and CRESST, University of Maryland, College Park, MD 20742, USA
[5] Dipartimento di Fisica, Università di Roma Tor Vergata, Via della Ricerca Scientifica 1, I-00133 Roma, Italy
[6] NASA Goddard Space Flight Center, Greenbelt, MD 20771, USA
[7] Wyle Science, Technology and Engineering Group, 1290 Hercules Avenue, Houston, TX 77058, USA
[8] Max-Planck-Institute for Extraterrestrial Physics (MPE), Giessenbachstrasse 1, D-85748, Garching, Germany
[9] Departamento de Física y Matemáticas, Universidad de Alcalá, Campus Universitario, E-28871 Alcalá de Henares, Madrid, Spain
[10] Naval Research Laboratory, Remote Sensing Division, 4555 Overlook Avenue SW, Washington, DC 20375, USA
[11] Department of Physics, Rhodes College, Memphis, TN 38112, USA
Received 2017 March 1; revised 2017 May 10; accepted 2017 May 30; published 2017 June 27

Abstract

In Tombesi et al., we reported the first direct evidence for a quasar accretion disk wind driving a massive ($>100\,M_\odot\,\mathrm{yr}^{-1}$) molecular outflow. The target was F11119+3257, an ultraluminous infrared galaxy (ULIRG) with unambiguous type 1 quasar optical broad emission lines. The energetics of the accretion disk wind and molecular outflow were found to be consistent with the predictions of quasar feedback models where the molecular outflow is driven by a hot energy-conserving bubble inflated by the inner quasar accretion disk wind. However, this conclusion was uncertain because the mass outflow rate, momentum flux, and mechanical power of the outflowing molecular gas were estimated from the optically thick OH 119 μm transition profile observed with *Herschel*. Here, we independently confirm the presence of the molecular outflow in F11119+3257, based on the detection of $\sim\pm1000\,\mathrm{km\,s}^{-1}$ blue- and redshifted wings in the CO(1−0) emission line profile derived from deep ALMA observations obtained in the compact array configuration ($\sim2\farcs8$ resolution). The broad CO(1−0) line emission appears to be spatially extended on a scale of at least ∼7 kpc from the center. Mass outflow rate, momentum flux, and mechanical power of (80–200) $R_7^{-1}\,M_\odot\,\mathrm{yr}^{-1}$, (1.5–3.0) $R_7^{-1}\,L_{\rm AGN}/c$, and (0.15–0.40)% $R_7^{-1}\,L_{\rm AGN}$, respectively, are inferred from these data, assuming a CO-to-H_2 conversion factor appropriate for a ULIRG (R_7 is the radius of the outflow normalized to 7 kpc, and $L_{\rm AGN}$ is the AGN luminosity). These rates are time-averaged over a flow timescale of 7×10^6 yr. They are similar to the OH-based rates time-averaged over a flow timescale of 4×10^5 yr, but about a factor of 4 smaller than the local ("instantaneous"; $\lesssim10^5$ yr) OH-based estimates cited in Tombesi et al. The implications of these new results are discussed in the context of time-variable quasar-mode feedback and galaxy evolution. The need for an energy-conserving bubble to explain the molecular outflow is also reexamined.

Key words: galaxies: active – galaxies: evolution – ISM: jets and outflows – quasars: general – quasars: individual (F11119+3257)

1. Introduction

Rapidly accreting supermassive black holes (SMBHs) produce tremendous amounts of radiative energy. The coupling of this energy with gas near the black hole or at larger scales in the host galaxy produces outflows of gas. These "quasar-mode" outflows are distinct from "radio-mode" jets in that they are much less collimated and therefore have the potential to impact a much greater swath of a galaxy's gas. Quasar-mode outflows are often invoked to play a fundamental role in the evolution of both SMBHs and their host galaxies, quenching star formation and explaining the tight SMBH–galaxy relations (e.g., Veilleux et al. 2005; Fabian 2012). Recent observations of large-scale neutral and molecular outflows in (U)LIRGs have provided supporting evidence for this idea, as they directly trace the gas out of which stars form (e.g., Feruglio et al. 2010, 2015; Fischer et al. 2010; Alatalo et al. 2011, 2015; Rupke & Veilleux 2011, 2013a, 2013b, 2015; Sturm et al. 2011; Veilleux et al. 2013, hereafter V13; Aalto et al. 2012, 2015; Cicone et al. 2014; González-Alfonso et al. 2014, 2017; García-Burillo et al. 2015; Lindberg et al. 2016). Theoretical models suggest an origin of these outflows as energy-conserving flows driven by fast active galactic nucleus (AGN) accretion disk winds (e.g., Faucher-Giguère & Quataert 2012; Zubovas & King 2012, 2014; Costa et al. 2014; Nims et al. 2015; Gaspari & Sadowski 2017).

Our previous claims of a connection between large-scale molecular outflows and AGN activity in (U)LIRGs were based on the fact that systems with quasar-like AGN luminosities host the faster and more powerful outflows (V13; Rupke & Veilleux 2013a; Cicone et al. 2014). Until recently, these claims were incomplete because they were lacking the detection of the putative inner wind. Conversely, studies of powerful AGN accretion disk winds to date had focused only on X-ray observations of local radio-quiet and radio-loud AGNs and a few higher-redshift quasars, but had ignored the impact of these winds on the galaxy host (e.g., Tombesi et al. 2010, 2014; Nardini et al. 2015 and references therein).

This situation changed with the publication of Tombesi et al. (2015, hereafter T15), where we showed the clear (6.5σ) detection of a powerful AGN accretion disk wind with a mildly

relativistic velocity of $\sim 0.25c$ in the X-ray spectrum of IRAS F11119+3257, a nearby ($z = 0.190$; $1'' = 3.19$ kpc) optically classified type 1 ULIRG hosting a powerful molecular outflow with velocity $V_{\rm out,OH} = 1000 \pm 200$ km s^{-1}. This was the first *direct* evidence for a fast quasar accretion disk wind driving a large-scale molecular outflow.[12] The energetics of the accretion disk wind and molecular outflow derived from our data are consistent with the energy-conserving mechanism (T15). In this scenario, the violent interaction of the fast inner AGN wind with the ISM of the host results in shocked wind gas that does *not* efficiently cool, but instead expands adiabatically as a hot bubble (e.g., Faucher-Giguère & Quataert 2012; Zubovas & King 2012, 2014; Costa et al. 2014; Nims et al. 2015). The adiabatically expanding shocked wind sweeps up gas and drives an outer shock into the host ISM. The outflowing gas cools radiatively, and most of it "freezes out" into clumps of cold molecular material. This picture is also able to explain the existence of a fast ($\sim$1300 km s^{-1}) neutral-atomic (Na I D) outflow in this system (Rupke et al. 2005a). A variant on this scenario is that preexisting molecular clouds from the host ISM are entrained in the adiabatically expanding shocked wind, accelerated to the observed velocities without being destroyed by the many erosive forces and instabilities (e.g., Cooper et al. 2009; McCourt et al. 2015, 2016; Scannapieco & Brüggen 2015; Thompson et al. 2015, 2016; Banda-Barragán et al. 2016; Tanner et al. 2016; Scannapieco 2017).

While the existence of the molecular outflow in F11119+3257 is unquestionable based on the OH absorption profile, the energetics of this outflow remain uncertain. In T15, we cite a mass outflow rate $\dot{M}_{\rm out,OH} = 800^{+1200}_{-550}\ M_\odot$ yr^{-1}, a momentum flux log $\dot{P}_{\rm out,OH} = 36.7 \pm 0.5$ in dynes, and a mechanical power log $\dot{E}_{\rm out,OH} = 44.4 \pm 0.5$ in erg s^{-1}. The large uncertainties stem mainly from the high optical depth of the OH 119 μm line and the lack of higher-excitation line profiles (e.g., OH 65 and 84 μm), and to some degree from the fact that the OH outflow is not spatially resolved in the *Herschel* data. In T15, we had to compare the predictions of our radiative transfer models (e.g., González-Alfonso et al. 2014) with the observed velocity-resolved profile of OH 119 μm to constrain the location (0.1–1.0 kpc) of the OH molecules that produce the OH profile. The energetics of the OH outflow scale linearly with the OH abundance $X_{\rm OH} = {\rm OH/H}$.[13] It is also important to note that the energetics cited in T15 are the local ("instantaneous") quantities estimated at a radius $R_{\rm out,OH} = 300$ pc. These values are time-averaged over $\Delta R_{\rm out,OH}/V_{\rm out,OH} \lesssim 10^5$ yr, the time the outflowing shell of material takes to cross the shell thickness $\Delta R_{\rm out,OH} \sim 75$ pc. The values time-averaged over the flow timescale $R_{\rm out,OH}/V_{\rm out,OH}$ are smaller by a factor of 4.

In the present paper, we take a complementary approach to constrain the energetics of the molecular outflow in F11119+3257, using line emission from low-level transitions of CO as a tracer of the outflowing molecular material. IRAM 30 m observations by Xia et al. (2012) have already shown that the CO(1−0) emission in F11119+3257 is broad (FWHM $\sim 285 \pm 36$ km s^{-1}), is centered on redshift $z_{\rm CO} = 0.190$, and has a luminosity of 1.12×10^{10} K km s^{-1} pc^2, corresponding to a molecular gas mass of $\sim 9 \times 10^9\ M_\odot$ for a Galactic conversion factor of $\alpha_{\rm CO} = 4.3\ M_\odot$ (K km s^{-1} pc^2)$^{-1}$. Our new ALMA data are considerably more sensitive than the IRAM data and reveal faint broad wings in the CO(1−0) line emission profile. Section 2 describes the ALMA observations of F11119+3257. The results from the analysis of these data are presented in Section 3 and compared with those of T15 in Section 4. The main conclusions are summarized in Section 5. Throughout this paper, we adopt a redshift $z = 0.190$ (Rupke et al. 2005a; Xia et al. 2012; D. S. N. Rupke et al. 2017, in preparation), a luminosity distance of 933 Mpc, and a corresponding linear scale of 3.19 kpc per arcsecond for F11119+3257 (using $H_0 = 69.6$ km s^{-1} Mpc^{-1}, $\Omega_M = 0.286$, and $\Omega_\Lambda = 0.714$ from Bennett et al. 2014).

2. ALMA Observations and Data Reduction

F11119+3257 was observed for 1.9 hr (on-source, 3.2 hr in total) on 2016 January 3 and 10 as part of project 2015.1.00305.S in Cycle 3. The observations were carried out with 36 antennas in the compact C36-1 12 m array configuration with baselines 15–312 m, resulting in an angular resolution of $\sim 2\farcs8 \sim 9$ kpc. The main objective of these observations was to detect the molecular outflow based on the presence of broad wings in the CO(1−0) line emission at 96.9 GHz (Band 3). An rms (1σ) sensitivity of 140 μJy in each 100 km s^{-1} channel was targeted, corresponding to 0.7% of the peak flux density measured by Xia et al. 2012 (4 mK $\sim$ 20 mJy). The CO(1−0) wing-to-peak ratios in (U)LIRGs (e.g., Cicone et al. 2014) are typically $\sim$5%, or 1.0 mJy $\sim 7\sigma$ for F11119+3257. A similar result is obtained if one assumes that the CO outflow luminosity is roughly proportional to the OH outflowing mass. For this exercise, we use an OH-to-CO scaling factor to translate the OH 119 μm equivalent width into CO(1−0) line flux based on the average observed relation in the outflows of ULIRGs Mrk 231, IRAS F08572+3915, and IRAS F10565+2448 (the scatter in the relation is $\sim$30%; Figure 2 in González-Alfonso et al. 2017). Only the blue wing ($\leqslant -200$ km s^{-1}) of the OH line equivalent width (i.e., only the truly outflowing component) is used for this calculation.

The requested angular resolution ($\sim 3''$ $\sim$ 9–10 kpc) and largest angular scale ($\sim 15''$–$20''$) of these objects safely allow complete CO(1−0) flux recovery from this galaxy (broad wings + bright core emission near systemic velocity; Xia et al. 2012). The correlator setup was optimized to simultaneously observe CO(1−0) and the adjacent continuum emission. The central frequency of baseband-4 was adjusted so that baseband-4 was contiguous with baseband-3 and also covered "for free" the CN (1−0) complex at 113.15 and 113.50 GHz and the SiO $v = 0$ (3−2), $v = 1$ (3−2), and $v = 2$ (3−2) transitions at 130.269, 129.363, and 128.459 GHz, respectively, possible tracers of shocked molecular gas in this galaxy. Spectral smoothing by a factor of 4 was used to reduce the data rate while maintaining a reasonable velocity resolution of $\sim$6 km s^{-1}. The pipeline-calibrated interferometric visibilities delivered by ALMA were continuum-subtracted in the *uv* plane using a first-order polynomial and then imaged at 20 km s^{-1} resolution using Briggs weighting with a robust parameter of 0.5 and cleaned using a tight box around the source. The restoring beam is $3\farcs46 \times 2\farcs21$ FWHM with PA = 12°.

[12] Since the publication of T15, Feruglio et al. (2015) have reported the tentative detection of a $\sim 0.1c$ X-ray wind in Mrk 231 at the 3.5σ level (see also Reynolds et al. 2017).

[13] Note, however, that the OH abundance adopted in T15, $X_{\rm OH} = 2.5 \times 10^{-6}$, is, within a factor of $\sim$3, consistent with the value inferred in the Galactic Sgr B2, the Orion KL outflow, and in buried galaxy nuclei, as well as with the predictions of chemical models of dense photodissociation regions and of cosmic-ray- and X-ray-dominated regions (see González-Alfonso et al. 2017).

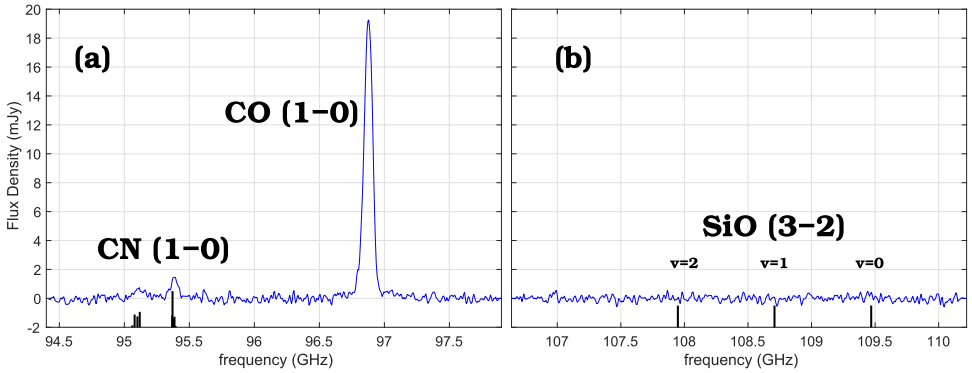

Figure 1. Full continuum-subtracted USB spectrum integrated inside a 3″-radius circular aperture: (a) 94.4–97.9 GHz, (b) 106.6–110.2 GHz. Channels are 20 km s^{-1} wide, but Hanning velocity smoothing was carried out to provide a spectral resolution of ∼40 km s^{-1}. The vertical black lines in panel (a) show the expected positions for the CN (1−0) hyperfine components, with the relative intensities observed in Orion (Turner & Gammon 1975). The SiO $v = 0$ (3−2), $v = 1$ (3−2), and $v = 2$ (3−2) transitions are not detected in panel (b).

3. Results

Figure 1 shows the full continuum-subtracted upper sideband (USB) spectrum extracted from within a circular 3″-radius aperture centered on the source. The channels are 20 km s^{-1} wide, but Hanning velocity smoothing was carried out to provide a spectral resolution of ∼40 km s^{-1}. The cube has a noise of 0.28 mJy in the 20 km s^{-1} channels. The strong CO(1−0) line emission is detected with a signal-to-noise ratio (S/N) of ∼65 at the peak. The hyperfine components of CN (1−0) at 113.15 and 113.50 GHz are also detected. On the other hand, the SiO $v = 0$, 1, and 2 (3−2) transitions at 130.269, 129.363, and 128.459 GHz are not visible in our band-4 data, so they are not discussed any further in the remainder of the paper.

Figure 2 zooms in on the CO(1−0) line emission within circular apertures with radii of 3″ and 5″ centered on F11119 +3257. Broad-line emission indicative of an outflow is detected in both panels out to velocities ∼±1000 km s^{-1} relative to systemic ($z = 0.190$), remarkably similar to the velocity of the OH outflow reported in T15. Three methods are used to quantify the strength of this broad emission.

First, we carry out a simultaneous fit for two Gaussians (one narrow, one broad) to these data. The broad Gaussian is shown as the yellow area in Figure 2. The residuals are generally less than ±0.5 mJy. The quantities derived from these fits are listed in Table 1. The uncertainties on these quantities were estimated using a bootstrap Monte Carlo method. Note that the broad-to-narrow peak flux ratios (∼3%–4%) listed in that table are similar to those assumed for the requested ALMA time (∼5%; Section 2). The fact that the broad-to-narrow integrated flux ratio is larger in the 5″-radius aperture spectrum (0.19) than in the 3″-radius aperture spectrum (0.14) suggests that the broad-line emission extends out to a radius of 5″, although the 5″ spectrum is noticeably more noisy than the 3″ spectrum. The fluxes of the broad components derived from these fits are considered upper limits to the actual flux from the outflowing material since they include CO line emission at low velocities that may not be associated with the outflow. We attempt to remove this low-velocity material using a different strategy.

Figure 3 reproduces the continuum-subtracted CO (1−0) spectrum integrated over a circular aperture with a radius of 3″. The red line shows the original spectrum (cut off vertically to show the details in the wings of CO(1−0)). The blue line

Table 1
Measured Quantities from Two-Gaussian Fits of the Integrated CO(1−0) Emission

Component	$V_{central}$ (km s^{-1})	FWHM (km s^{-1})	Integrated Flux (Jy km s^{-1})	Peak Flux (mJy)
(1)	(2)	(3)	(4)	(5)
3″-radius Aperture				
Narrow Gaussian	−32 ± 2	226 ± 4	4.63 ± 0.07	19.03 ± 0.25
Broad Gaussian	−11 ± 53	1113 ± 171	0.66 ± 0.07	0.55 ± 0.14
5″-radius Aperture				
Narrow Gaussian	−32 ± 2	224 ± 4	5.14 ± 0.10	21.33 ± 0.25
Broad Gaussian	+47 ± 48	1068 ± 168	0.98 ± 0.10	0.86 ± 0.18

shows the residuals after fitting and removing a Gaussian source model to each 20 km s^{-1} channel. First, a two-dimensional Gaussian was fit to the image for each channel in the region where a source is detected. The results were then used to make a smooth source model with linearly changing position as a function of velocity (to account for a possible velocity gradient; see below), Gaussian-changing intensity, but constant size and orientation. This smooth source model was then removed from each velocity slice to arrive at a "residuals" cube. The high S/N of the detection allows us to centroid the source in each channel with very good sub-beam precision. The velocity gradient measured is +350 km s^{-1} kpc^{-1} in right ascension and −200 km s^{-1} kpc^{-1} in declination (Figure 4). This compares well with the direction and amplitude of the velocity gradient measured in an unpublished Keck laser guide star adaptive optics Paα data cube of F11119+3257 obtained with OSIRIS (D. S. N. Rupke 2017, private communication). Assuming that this represents the rotation of the gas in the host galaxy, a dynamical mass of $\sim 5 \times 10^9\, M_\odot$ within ∼1 kpc from the center is derived from these data.

The yellow region in Figure 3 shows the CO "high-velocity" emission, which cannot be accounted for by the gas in pure rotation. Figure 5 shows maps of the rotating material and high-velocity gas integrated over the "residuals" channels shown in

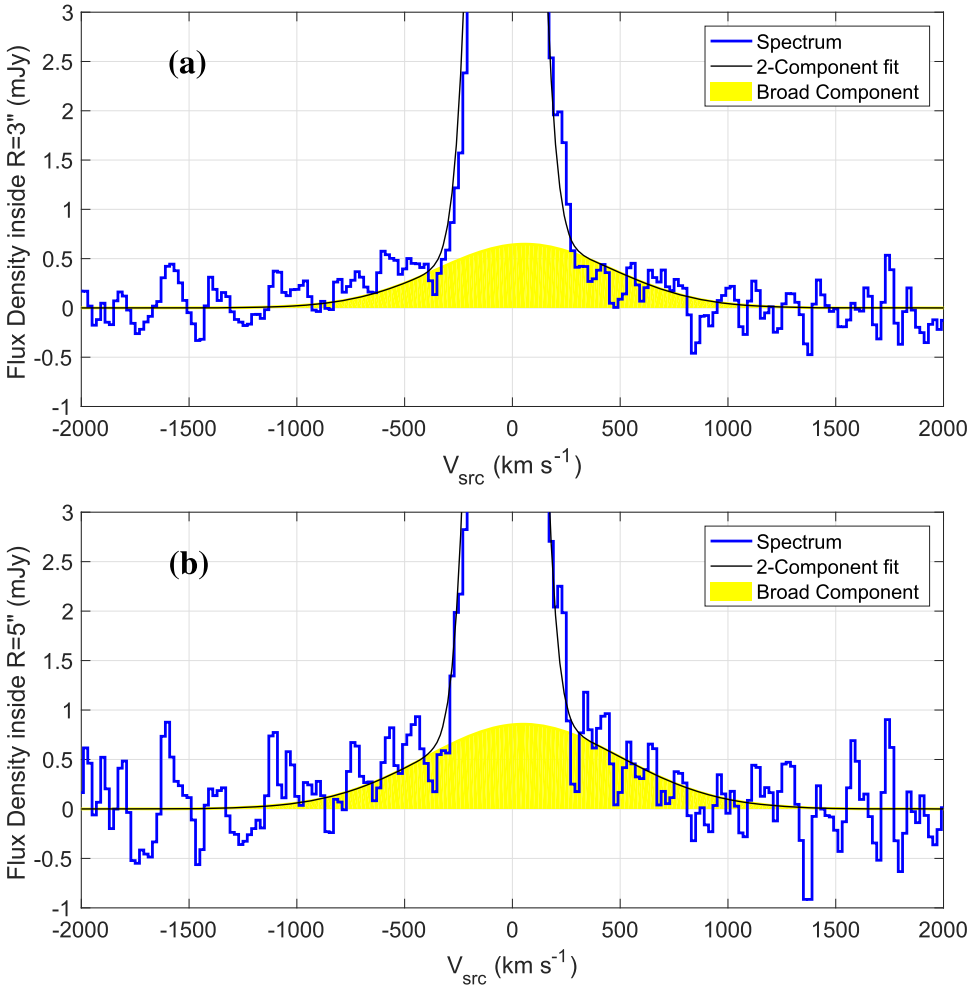

Figure 2. Simultaneous two-Gaussian fit to the CO(1−0) line emission within (a) a 3″-radius circular aperture centered on F11119+3257 and (b) a 5″-radius circular aperture centered on F11119+3257. The CO fluxes in the broad and narrow components are listed in Table 1.

Table 2
Measured Quantities from Residual Map after Removal of the Rotating Disk

Component	Velocity Range (km s^{-1})	Integrated Flux (Jy km s^{-1})	Size (FWHM)[a] (arcsec)	R.A. Offset (arcsec)	Decl. Offset (arcsec)
(1)	(2)	(3)	(4)	(5)	(6)
Blue + red wings	[−820, −400], [+280, +800]	0.40 ± 0.10	(5.1 × 2.8) ± 0.1	+0.22 ± 0.05	−0.75 ± 0.10

Note.
[a] Not corrected for the beam size (3.″46 × 2.″21 FWHM).

yellow in Figure 3. Table 2 lists the parameters derived from Figure 5(c). The high-velocity gas is extended and offset by $+0.''22 \pm 0.''05$ in right ascension and $-0.''75 \pm 0.''10$ in declination from the USB band-4 continuum emission (shown in Figure 1(b)). A Gaussian fit to the high-velocity line emission image of Figure 3 finds an FWHM size of $5.''1 \times 2.''8$ with $0.''1$ uncertainty in either direction, elongated along PA = 4° from the north–south direction; this is significantly larger than the $3.''46 \times 2.''21$ FWHM beam.

Aperture photometry on the high-velocity gas confirms that it is indeed extended. In Figure 6, the enclosed high-velocity integrated flux peaks around a radius of $5'' \pm 1.''5$ and then remains roughly constant around $\sim 0.4 \pm 0.1$ Jy km s^{-1}. This is our conservative estimate for the flux from the molecular outflow. The uncertainty on the enclosed flux is estimated from the amplitude of the fluctuations around the value of 0.4 Jy km s^{-1} observed in Figure 6. A radius of $5'' \pm 1.''5$ on the image corresponds to an actual radius of $4.''8^{+1.5}_{-2.7}$, after correcting for the beam size ($3.''46 \times 2.''21$ FWHM, i.e., $\sim 2.''8$ FWHM). This radius, $4.''8^{+1.5}_{-2.7} = 15^{+5}_{-8}$ kpc, is our best estimate of the maximum extent of the CO outflow.

As an independent check on the results from our analysis of these imaging data, we also derived the sizes and fluxes of the wing emission by fitting the data directly in the *uv* plane. For this exercise, we used both the CASA *uv*-Plane Model Fitting routine *uvmodelfit* and *uvmultifit*, the library of Martí-Vidal et al. (2014). The results are summarized in Table 3. In contrast to *uvmodelfit*, *uvmultifit* could not deal with the sum of the red

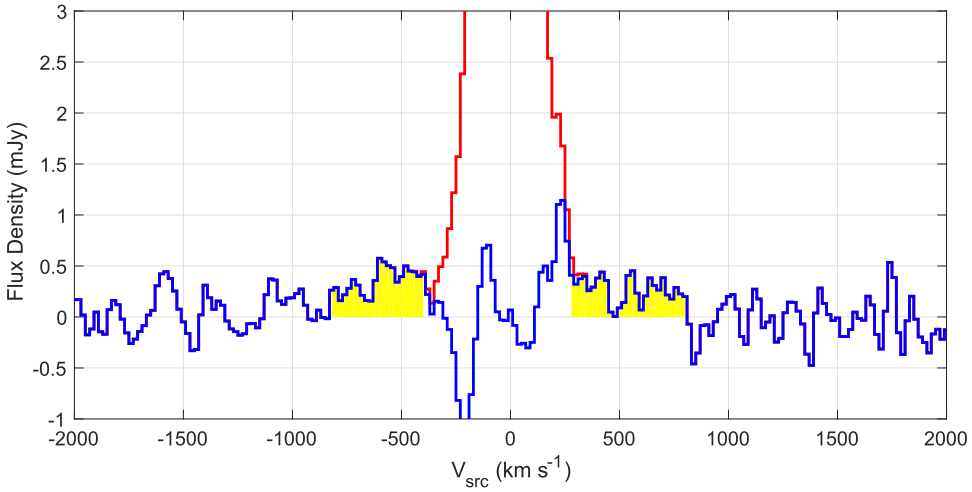

Figure 3. Same as Figure 2(a), but here the blue line shows the residuals after fitting and removing a two-dimensional Gaussian source model to each 20 km s^{-1} channel, representative of the gas in pure rotation. See text in Section 2 for more details on the removal method. The yellow region shows the high-velocity emission in CO, from −820 to −400 km s^{-1} and from +280 to +800 km s^{-1}, which cannot be accounted for by the gas in pure rotation.

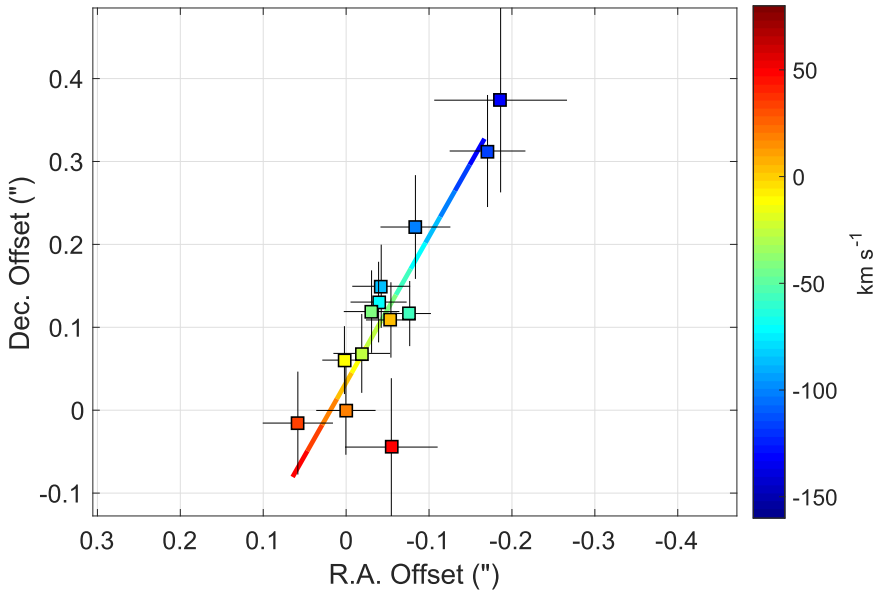

Figure 4. Velocity gradient due to rotation in the host galaxy derived from the ALMA CO (1–0) line emission. The linear scale is 3.19 kpc per arcsecond. See Section 2 for more details on the derivation.

and blue wings, so they were fit separately. The signals were integrated between 96.9893 and 97.1315 GHz (−820 to −380 km s^{-1}) for the blue wing and between 96.6081 and 96.7244 GHz for the red wing (+440 to +800 km s^{-1}). As shown in Figure 3, these channels are not affected by rotation, so we did not have to remove a disk model in the *uv* plane fitting. The results from the two *uv* fitters are consistent with each other and with the results from the imaging methods (compare the entries in Table 3 with those of Tables 1 and 2).

Taken at face value and keeping in mind the large uncertainties on these estimates, the CO outflow in F11119+3257 is the largest molecular outflow so far detected in a local ULIRG: $R_{\rm out,CO}$ is typically ∼1 kpc in these objects with the possible exceptions of F23060+0505 and Mrk 876, where the CO outflows are not well resolved and imply $R_{\rm out,CO} \leqslant$ 4.05 kpc and ⩽3.55 kpc, respectively (Cicone et al. 2014), and F08572+3915, where a fast-moving (∼1000 km s^{-1}) cloud was recently detected by A. W. Janssen et al. (2017, in preparation) at ∼6 kpc from the NW galaxy. Nothing in the galaxy host of F11119+3257 itself (Kim et al. 2002; Veilleux et al. 2002) can account for the morphology and kinematics of this broad CO line emission. The implications of these results are discussed in the following section.

4. Discussion

4.1. Energetics of the CO Outflow

The mass of molecular gas involved in the outflow can be derived from the integrated flux densities quoted in the previous section (0.3–1.0 Jy km s^{-1}), using Equation (3) from Bolatto et al. 2013b). A Galactic CO-to-H_2 conversion factor $X_{\rm CO} = 2 \times 10^{20}$ cm^{-2} (K km s^{-1})$^{-1}$ (or equivalently $\alpha_{\rm CO} =$ 4.3 $M_\odot$ (K km s^{-1} pc^2)$^{-1}$) would imply a CO-based molecular mass $M_{\rm out,CO} = (3–8) \times 10^9\,M_\odot$, given a luminosity distance of 933 Mpc. A conservative lower limit on the outflowing molecular gas mass $M_{\rm out,CO} \sim (2–6) \times 10^8\,M_\odot$ is derived if

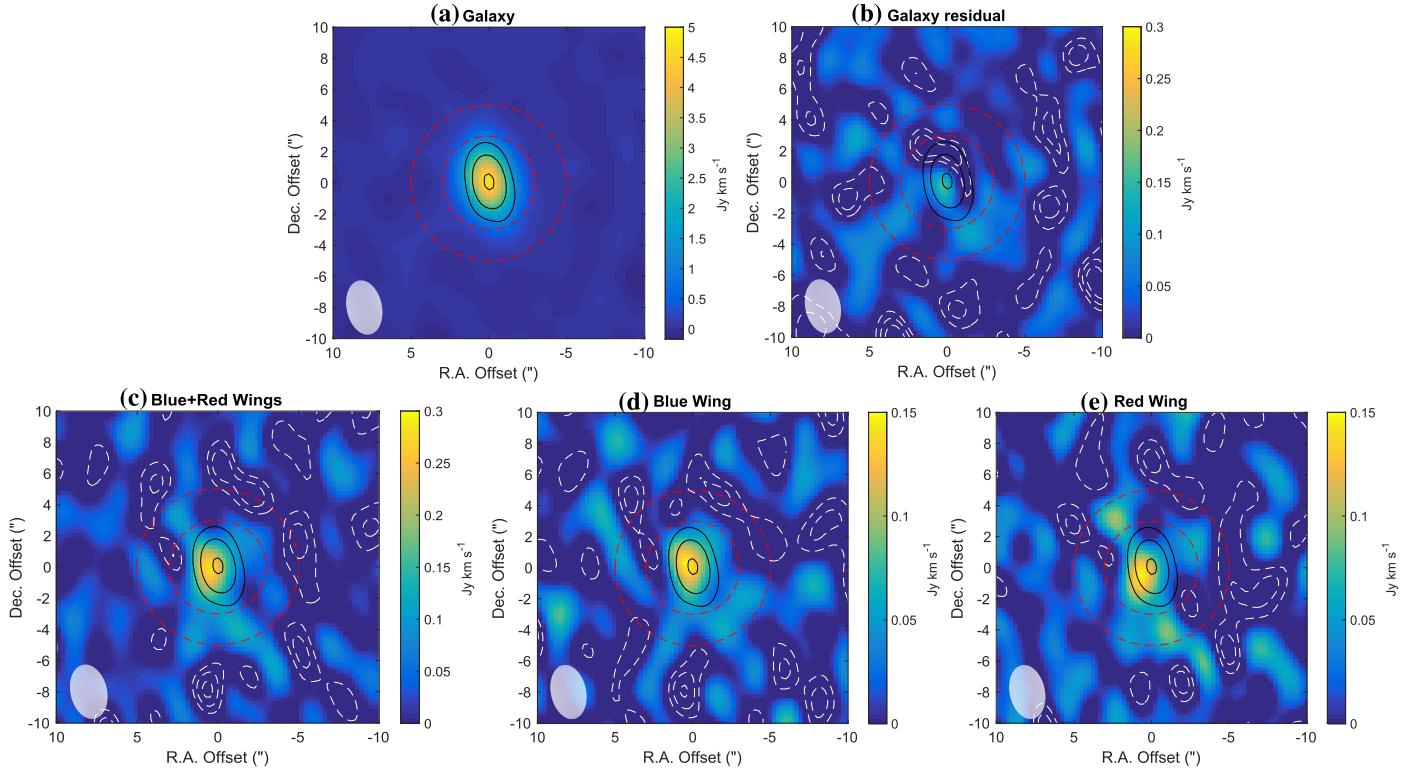

Figure 5. Maps of the CO(1–0) emission from the various kinematic components of F11119+3257: (a) the rotating disk; (b) "residuals" channels between −400 and +280 km s^{-1} after subtraction of the rotating material; (c) blue + red wings, i.e., the "residual" channels between −820 and −380 km s^{-1} and between +280 and +800 km s^{-1}; (d) blue wing only, i.e., between −820 and −380 km s^{-1}; (e) red wing only, i.e., between +280 and +800 km s^{-1}. The linear scale is 3.19 kpc per arcsecond. For each panel, the color scale on the right indicates the flux level (note that the panels are on different scales). The white contours indicate −1, −2, and −3× the rms noise (=0.033, 0.033, 0.04, 0.026, and 0.029 Jy km s^{-1} for panels (a), (b), (c), (d), and (e), respectively). The black contours show the USB continuum emission (0.1, 0.25, and 0.5 mJy). The beam size is shown in the lower left corner of each panel, and the 3″- and 5″-radius circular apertures centered on the CO peak are shown as red dashed circles. Note that the emission from the high-velocity gas is extended and offset from the continuum emission and the rotating disk.

we use the ∼13× smaller optically thin X_{CO} used by Bolatto et al. (2013a) to estimate the outflowing molecular gas mass in NGC 253. A compromise between these two extremes is to adopt a ULIRG-like α_{CO} of 0.8 $M_\odot$ (K km s^{-1} pc^2)$^{-1}$ as done by Cicone et al. (2014). This results in an outflowing molecular gas mass of ∼(0.6–1.4) × 10^9 $M_\odot$, which falls at the high-mass end of the spectrum covered by local ULIRGs (Cicone et al. 2014; González-Alfonso et al. 2017). For comparison, the non-outflowing material emits 5–6 Jy km s^{-1} in CO(1−0). Assuming the same ULIRG-like X_{CO} as for the outflowing material, the amount of quiescent molecular gas in the host galaxy is $M_{host,CO}$ ∼ (7–10) × 10^9 $M_\odot$, i.e., in the top quartile of local ULIRGs and infrared quasars (e.g., Solomon et al. 1997; Evans et al. 2001, 2006; Scoville et al. 2003; Xia et al. 2012), and about 5–15× the amount in the CO outflow.

The next step is to derive the CO-based mass outflow rate $\dot{M}_{out,CO}$, momentum flux $\dot{P}_{out,CO}$, and mechanical power $\dot{E}_{out,CO}$ of the molecular outflow of F11119+3257. As discussed in detail in Rupke et al. (2005b) and González-Alfonso et al. (2017), there are two limiting approaches to the estimation of the outflow energetics: the local or instantaneous (maximum) values and the average (minimum) values. The local or instantaneous values are time-averaged over the timescale taken by the outflow shell of material to cross the thickness of the shell. This first approach was used in Sturm et al. (2011), González-Alfonso et al. (2014), and T15. Here, we use instead the most conservative $\dot{M}_{out}$, $\dot{P}_{out}$, and $\dot{E}_{out}$ values based on the second approach to characterize the outflow of F11119+3257. In that case, we have

$$\dot{M}_{out,CO} = \frac{M_{out,CO}\ V_{out,CO}}{R_{out,CO}}, \quad (1)$$

$$\dot{P}_{out,CO} = \dot{M}_{out,CO}\ V_{out,CO}, \quad (2)$$

$$\dot{E}_{out,CO} = \frac{1}{2}\dot{M}_{out,CO} V^2_{out,CO}. \quad (3)$$

These correspond to the "time-averaged thin shell" values of Rupke et al. (2005b), time-averaged over the flow timescale $R_{out,CO}/V_{out,CO}$, and have been used extensively to describe the energetics of the ionized and neutral phases of outflows (e.g., Arav et al. 2013; Borguet et al. 2013; Rupke & Veilleux 2013a; Heckman et al. 2015), as well as some molecular outflows (González-Alfonso et al. 2017). They are most appropriate for comparison with outflow models (e.g., Faucher-Giguère & Quataert 2012; Thompson et al. 2015; Stern et al. 2016). In some studies (e.g., Feruglio et al. 2010, 2015; Maiolino et al. 2012; Rodríguez Zaurín et al. 2013; Cicone et al. 2014; Harrison et al. 2014; García-Burillo et al. 2015), a factor of 3 higher values have been used under the assumption that the emitting spherical (or multiconical) volume is filled with uniform density. However, for a steady mass-conserving flow with constant velocity, we would expect a density at the outer radius only 1/3 that of the average, thus also yielding the expression in Equation (1). The quick drop-off in the radial intensity profile of the outflow emission of F11119+3257 indeed seems consistent with this picture. Thus, we adopt Equations (1)–(3) for the rest of the discussion.

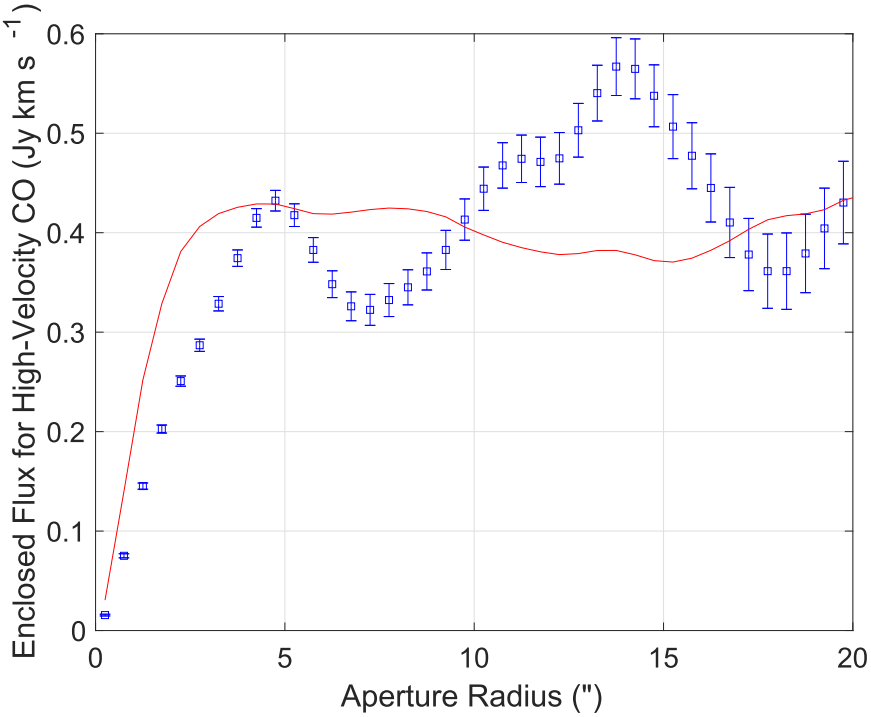

Figure 6. Aperture photometry on the high-velocity CO (1−0) emission shown in Figures 3 and 5. The integrated high-velocity CO line flux is plotted in blue as a function of the radius of the circular aperture. For comparison, the integrated continuum flux, which is unresolved, is shown in red. The flux peaks around $R = (5 \pm 1.5)''$ and then stays around $\sim 0.4 \pm 0.1$ Jy km s^{-1}. A radius of $(5 \pm 1.5)''$ measured on the image corresponds to an actual radius of $4\farcs8^{+1.5}_{-2.7} = 15^{+5}_{-8}$ kpc after correcting for the beam size—this is our best estimate of the maximum extent of the CO outflow.

Table 3
Measured Quantities from *uv* Plane Fitting

Component	Velocity Range (km s^{-1})	Integrated Flux (Jy km s^{-1})	Size (FWHM) (arcsec)	R.A. Offset (arcsec)	Decl. Offset (arcsec)
(1)	(2)	(3)	(4)	(5)	(6)
		Fitter: *uvmodelfit*			
Blue + red wings	[−820, −380], [+440, +800]	0.31 ± 0.05	3.9 ± 1.0	+0.12 ± 0.21	−0.44 ± 0.30
		Fitter: *uvmultifit*			
Blue wing	[−820, −380]	0.22 ± 0.08	3.8 ± 2.0	−0.35 ± 0.5	−0.03 ± 0.60
Red wing	[+440, +800]	0.14 ± 0.07	5.4 ± 3.5	+0.2 ± 0.7	−0.98 ± 1.20

Our choice of $R_{\rm out,CO}$ and $V_{\rm out,CO}$ will set the flow timescale ($R_{\rm out,CO}/V_{\rm out,CO}$) in these expressions and therefore has to be done with care. If, for instance, we set $R_{\rm out,CO}/V_{\rm out,CO} = R^{\rm max}_{\rm out,CO}/V^{\rm max}_{\rm out,CO}$, where $R^{\rm max}_{\rm out,CO}$ is the maximum extent of the outflow ($\sim$15 kpc; Section 3) and $V^{\rm max}_{\rm out,CO}$ is the maximum outflow velocity ($\sim$1000 km s^{-1}, ignoring projection effects), then the flow timescale $R_{\rm out,CO}/V_{\rm out,CO} \approx 1.5 \times 10^7$ yr. This value would underestimate the actual flow time if all of the outflowing gas originated from the center and was uniformly accelerated from rest. If this were the case, the flow timescale would be longer by a factor of $\sim$2 (González-Alfonso et al. 2017) and we would expect the material with the highest outflow velocities to be located farther from the center than the material with the lowest outflow velocities. While our data are not deep enough to allow us to detect any velocity gradient in the outflow emission (Figure 5), systematic positive radial velocity gradients have not been detected in the data of any other ULIRG (e.g., Cicone et al. 2014). Thus, we do not favor this longer flow timescale.

We argue instead for a smaller flow timescale given that our measurement of the full extent of the outflowing gas is uncertain and a significant fraction ($\gtrsim$50%) of the outflowing material is unresolved (Figure 5). If the outflow were in fact completely unresolved, $R_{\rm out,CO} \lesssim 4$ kpc and $R_{\rm out,CO}/V_{\rm out,CO} \lesssim 4 \times 10^6$ yr. The actual value of ($R_{\rm out,CO}/V_{\rm out,CO}$) most likely lies between these two extremes. In the following discussion, we adopt a conservatively low value for the radius, $R_{\rm out,CO} = 7$ kpc, and $V_{\rm out,CO} = 1000$ km s^{-1} (hence $R_{\rm out,CO}/V_{\rm out,CO} = 7 \times 10^6$ yr), as nominal values of the size and velocity of the CO outflow, and a ULIRG-like CO-to-H_2 conversion factor (we discuss the validity of the latter assumption in Section 4.3). From Equations (1)–(3) we get $\dot{M}_{\rm out,CO} = 80$–$200\ M_\odot$ yr^{-1}, $\dot{P}_{\rm out,CO} = (6$–$13) \times 10^{35}$ dynes $= (1.5$–$3.0) L_{\rm AGN}/c$, and $\dot{E}_{\rm out,CO} = (3$–$6) \times 10^{43}$ erg s^{-1} = (0.15−0.40)% $L_{\rm AGN}$, where $L_{\rm AGN} = 1.5 \times 10^{46}$ erg s^{-1}, derived from the infrared 15–30 μm color and the prescription of Veilleux et al. (2009). These numbers need to be scaled up by a factor of 5.3 if the CO-to-H_2 conversion factor is Galactic rather than ULIRG-like, or scaled down by a factor of 2.4 if CO(1−0) is optically thin. The results are summarized in Table 4.

Table 4
Derived Properties of the Small- and Large-scale Outflows in F11119+3257

Outflow Type (1)	Outflow Velocity (2)	Radius (Lower Limit) (3)	Radius (Upper Limit) (4)	Covering Fraction (5)	$\dot{M}$ ($M_\odot$ yr^{-1}) (6)	$\dot{P}$ (L_{AGN}/c) (7)	$\dot{E}$ (L_{AGN}) (8)
Accretion disk wind[a]	0.255 ± 0.011 c	$15r_s$	$900r_s$	>0.85	1.5–4.5[b]	0.4–3.0[c]	(6–50)%[d]
OH outflow (local)[e]	1000 ± 200 km s^{-1}	0.1 kpc	1.0 kpc	0.20 ± 0.05	250–2000[f]	3.5–25[g]	(0.5–5.0)%[h]
OH outflow (average)[i]	**1000 ± 200 km s^{-1}**	**0.1 kpc**	**1.0 kpc**	**0.20 ± 0.05**	**60–500[j]**	**1.0–6[g]**	**(0.1–1.0)%[h]**
CO outflow (ULIRG-like)[k]	**1000 ± 200 km s^{-1}**	**<4.0 kpc**	**15 kpc**	**<0.50[l]**	**80–200[m]**	**1.5–3[n]**	**(0.15–0.40)%[o]**
CO outflow (Galactic)[p]	1000 ± 200 km s^{-1}	<4.0 kpc	15 kpc	<0.50[l]	400–1000[m]	8–16[n]	(0.80–2.0)%[o]
CO outflow (optically thin)[q]	1000 ± 200 km s^{-1}	<4.0 kpc	15 kpc	<0.50[l]	30–90[m]	0.6–1.3[n]	(0.06–0.17)%[o]

Notes. Boldfaced entries indicate favored estimates. Column (1): this table lists the physical properties of three different outflows: (i) the X-ray wind on the scale of the accretion disk first reported in T15, (ii) the *Herschel*-detected OH outflow first reported in V13, and (iii) the ALMA-detected CO outflow reported in the present paper. Column (2): estimate of the outflow velocity. Column (3): lower limit on the size of the outflow. Column (4): upper limit on the size of the outflow. Column (5): estimate of the fraction of the sky covered by the outflowing material. Column (6): mass outflow rate in $M_\odot$ yr^{-1}. Column (7): momentum flux normalized to the radiation pressure, L_{AGN}/c. Column (8): mechanical power normalized to the AGN luminosity, $L_{AGN} = 1.5 \times 10^{46}$ erg s^{-1}, derived from the infrared 15–30 μm color and the prescription of Veilleux et al. (2009).

[a] Quantities derived from the *Suzaku* data of T15.

[b] $\dot{M}_{wind} = 1.5 \times (r_{wind}/15r_s)\,(N_H/6.4 \times 10^{24}\ cm^{-2}) \times (C_{f,wind}/1.0) \times (V_{wind}/0.255c)\ M_\odot\ yr^{-1}$, where r_{wind} is the wind radius, r_s is the Schwarzschild radius of the SMBH in F11119+3257 ($M_{BH} = 1.6 \times 10^7\ M_\odot$; Kawakatu et al. 2007), N_H is column density of the (fully ionized) wind, and $C_{f,wind}$ is the wind covering fraction.

[c] $\dot{P}_{wind} = \dot{M}_{wind} \times V_{wind}$.

[d] $\dot{E}_{wind} = \frac{1}{2}\,\dot{M}_{wind} \times V^2_{wind}$.

[e] Local ("instantaneous") quantities derived by T15 from the *Herschel* OH 119 μm presented in V13.

[f] $\dot{M}_{out,OH} = 800 \times (R_{out,OH}/300\ pc)^2 \times (n_H/100\ cm^{-3}) \times (C_{f,out,OH}/0.2) \times (V_{out,OH}/1000\ km\ s^{-1})\ M_\odot\ yr^{-1} = M_{out,OH}\ V_{out,OH}\ \Delta R^{-1}_{out,OH}$, where $R_{out,OH}$ is the radius of the OH outflow, n_H is the hydrogen number density, $C_{f,out,OH}$ is the OH outflow covering fraction, $M_{out,OH}$ is the total outflowing mass of molecular gas, and $\Delta R_{out,OH}$ is the thickness of the outflowing shell (=75 pc).

[g] $\dot{P}_{out,OH} = \dot{M}_{out,OH} \times V_{out,OH}$.

[h] $\dot{E}_{out,OH} = \frac{1}{2}\,\dot{M}_{out,OH} \times V^2_{out,OH}$.

[i] Time-averaged quantities derived from the *Herschel* OH 119 μm presented in V13.

[j] $\dot{M}_{out,OH} = 200 \times (R_{out,OH}/300\ pc) \times (N_H/2.3 \times 10^{22}\ cm^{-2}) \times (C_{f,out,OH}/0.2) \times (V_{out,OH}/1000\ km\ s^{-1})\ M_\odot\ yr^{-1} = M_{out,OH}\ V_{out,OH}\ R^{-1}_{out,OH}$, where $R_{out,OH}$ is the radius of the OH outflow, N_H is the hydrogen column density, $C_{f,out,OH}$ is the OH outflow covering fraction, and $M_{out,OH}$ is the total outflowing mass of molecular gas.

[k] Quantities derived from the ALMA CO(1−0) data using a ULIRG-like α_{CO} of 0.8 $M_\odot$ (K km s^{-1} pc^2)$^{-1}$.

[l] The covering fraction of the CO outflow is estimated from the patchiness of the high-velocity CO emission on large scales in Figure 5 (see Section 4.3 for more details).

[m] $\dot{M}_{out,CO} = 140\ (M_{out,CO}/1 \times 10^9\ M_\odot) \times (R_{out,CO}/7\ kpc)\ (V_{out,CO}/1000\ km\ s^{-1})^{-1}\ M_\odot\ yr^{-1}$.

[n] $\dot{P}_{out,CO} = \dot{M}_{out,CO} \times V_{out,CO}$.

[o] $\dot{E}_{out,CO} = \frac{1}{2}\,\dot{M}_{out,CO} \times V^2_{out,CO}$.

[p] Quantities derived from the ALMA CO(1−0) data using a Galactic $\alpha_{CO} = 4.3\ M_\odot$ (K km s^{-1} pc^2)$^{-1}$.

[q] Quantities derived from the ALMA CO(1−0) data using an optically thin $\alpha_{CO} = 0.34\ M_\odot$ (K km s^{-1} pc^2)$^{-1}$.

4.2. Comparisons with the Herschel OH Outflow

Table 4 compares the mass, momentum, and kinetic energy outflow rates derived from the new ALMA CO(1−0) data cube with the values derived from the spatially unresolved *Herschel* OH 119 μm spectral feature (V13; T15). As noted earlier, the measured velocity of the CO(1−0) outflow is remarkably similar to that of the OH outflow derived from the *Herschel* data. Note, however, that the scales probed by the two data sets are significantly different: modeling of the *Herschel* OH profile suggests a scale for the OH outflow of ~0.1–1.0 kpc (nominally 300 pc; T15), while the ALMA data show broad CO line emission possibly extending out to ~15 kpc. This difference in scale between the OH and CO outflows is not unexpected: OH absorption is produced by gas in front of the source of far-IR continuum, which is compact in ULIRGs, but there is no such requirement for the detection of the CO line emission. Moreover, CO(1−0) traces the more diffuse low-excitation molecular gas, from which there may not be excited absorption. This difference in scale is important since the dynamical parameters of the CO outflow listed in Table 4 are quantities that are time-averaged over a flow timescale $(R_{out,CO}/V_{out,CO}) \sim 7 \times 10^6$ yr, while the published OH-based mass outflow rate is a local ("instantaneous") estimate at $R_{out,OH} \sim 300$ pc, which is valid for timescales $(\Delta R_{out,OH}/V_{out,OH}) \lesssim 10^5$ yr, where $\Delta R_{out,OH} \approx 75$ pc, the thickness of the outflow shell of molecular material derived from the OH 119 μm profile. The second row in Table 4 lists the dynamical quantities time-averaged over the flow timescale $R_{out,OH}/V_{out,OH} = 4 \times 10^5$ yr; these quantities are $R_{out,OH}/\Delta R_{out,OH} = 4$ times smaller than the local quantities and comparable to the values derived from the CO outflow.

Given the well-known short- and long-term variability of F11119+3257 (T15) and AGNs in general (e.g., Schawinski et al. 2010, 2015; Keel et al. 2012a, 2012b, 2015, 2017), it is perhaps surprising to find in Table 4 that the time-averaged mass, momentum, and energy outflow rates derived from the CO data are similar to the time-averaged values derived from the OH data. This suggests that the efficiency of the quasar at driving the molecular outflow on large scales in F11119+3257 has been relatively stable

over the past few $\times$ 10^6 yr. We return to this issue in the next section.

4.3. Comparisons with Published Models

In T15, we argued that the dynamics of the X-ray wind and OH outflow were consistent with the models where the OH outflow is an energy-conserving flow driven by a fast AGN accretion disk wind (e.g., Faucher-Giguère & Quataert 2012; Zubovas & King 2012, 2014; Costa et al. 2014; Nims et al. 2015). If this is the case, we have by energy conservation

$$\dot{P}_{\rm out} = f\,(V_{\rm wind}/V_{\rm out})\;\dot{P}_{\rm wind} \quad (4)$$

$$\sim f\,(V_{\rm wind}/V_{\rm out})\;(L_{\rm AGN}/c), \quad (5)$$

where the quantities with subscript "out" refer to the molecular outflow, while those with subscript "wind" refer to the inner X-ray wind. The last equality (Equation (5)) is valid only if the inner wind is radiatively accelerated, i.e., $\dot{P}_{\rm wind} \sim L_{\rm AGN}/c$, which appears to be the case in F11119+3257 (T15; Table 4). The efficiency f is defined as the fraction of the kinetic energy in the X-ray wind that goes into bulk motion of the swept-up molecular material. In T15, an independent estimate of f was derived from the ratio of the covering fraction of the OH outflow ($C_{\rm f,out,OH}$) to that of the X-ray wind ($C_{\rm f,wind}$). In T15, we derived $C_{\rm f,wind} > 0.85$ from the X-ray data and $C_{\rm f,out,OH} = 0.20 \pm 0.05$ from the *Herschel* data, so $f = 0.22 \pm 0.07$. In T15, we showed that the above expression for energy conservation applies remarkably well to F11119+3257, to within the (admittedly large) uncertainties of the measurements.

Let us revisit this analysis using the new ALMA data. In the following discussion, we use the molecular mass, momentum, and energy outflow rates that are derived assuming a ULIRG-like CO-to-H_2 conversion factor of $\alpha_{\rm CO} = 0.8\,M_\odot\,({\rm K\,km\,s^{-1}\,pc^2})^{-1}$. We therefore make the implicit assumption that the physical state (e.g., density, temperature, metallicity, internal random/turbulent velocity, external radiation field, etc.) of the outflowing molecular gas in F11119+3257 is similar to that of the quiescent molecular material in the host ULIRG, from which it presumably originates. This issue is still a matter of debate, although the detection of high-density molecular gas entrained in the outflows of NGC 253 (Walter et al. 2017) and other ULIRGs (e.g., Mrk 231; Aalto et al. 2012, 2015) brings some support to this assumption. Given the supersolar metallicity and high total surface density of ULIRGs (e.g., Rupke et al. 2008; González-Alfonso et al. 2015), we expect $\alpha_{\rm CO}$ to be 2–5$\times$ smaller than the Galactic value (e.g., Bolatto et al. 2013b). We also naively expect a decrease in the CO(1−0) optical depth due to the likelihood of highly turbulent conditions in the emitting gas, but the detection of high-density molecular gas entrained in the outflow of NGC 253 favors a high column density (Walter et al. 2017) and seems to rule out the conservatively smaller optically thin $\alpha_{\rm CO}$ value of $0.34\,M_\odot\,({\rm K\,km\,s^{-1}\,pc^2})^{-1}$ used by Bolatto et al. 2013b). In the end, we feel that using a ULIRG-like $\alpha_{\rm CO}$ is the most realistic value for the outflowing molecular gas, given our current knowledge of the conditions in the outflowing material, and also a good compromise solution between the 5.3$\times$ higher values derived assuming Galactic $\alpha_{\rm CO}$ and the 2.4$\times$ smaller values based on optically thin $\alpha_{\rm CO}$ (Table 4).

Using the molecular momentum outflow rate based on the ULIRG-like $\alpha_{\rm CO}$ in Equation (4), we derive $f_{\rm CO} = 0.02$–0.03, considerably smaller than the value based on the OH outflow using the local estimates of the energetics ($f_{\rm OH} = 0.2$; T15), but comparable to the value we would derive if we use the time-averaged quantities of Table 4 ($f_{\rm OH} = 0.05$). In principle, an independent value of $f_{\rm CO}$ may be derived from the ratio of the covering fraction of the CO outflow ($C_{\rm f,out,CO}$) to that of the X-ray wind ($C_{\rm f,wind} > 0.85$; T15). However, in practice, the modest angular resolution of our ALMA data, taken in compact array configuration, provides only an upper limit on $C_{\rm f,out,CO}$ since the extended emission from the outflowing material seen in Figure 5 will likely break up into smaller cloudlets when observed at higher angular resolution (e.g., F08572+3915; Jannsen et al. 2017, in preparation), and therefore reduce $C_{\rm f,out,CO}$. We derive $C_{\rm f,out,CO} < 0.5$, and thus $f_{\rm CO} < 0.5$, from the morphology of the high-velocity CO emission on large scales in Figure 5.

Equations (4) and (5) are only valid if the molecular outflow is an adiabatic energy-driven flow. However, Table 4 shows that the molecular momentum outflow rate based on the ULIRG-like $\alpha_{\rm CO}$ is only a few times larger than the radiation pressure, $L_{\rm AGN}/c$, exerted by the AGN in F11119+3257 (Table 4). The starburst in F11119+3257 will contribute an additional term: $(1-\alpha_{\rm AGN})\;L_{\rm BOL}/c = [(1-\alpha_{\rm AGN})/\alpha_{\rm AGN}]\;L_{\rm AGN}/c \sim 0.25\;L_{\rm AGN}/c$ ($L_{\rm BOL}$ is the bolometric luminosity; Veilleux et al. 2009). A similar statement can be made when considering the time-averaged OH-based momentum outflow rate. Thus, the only time we need to invoke models of energy-conserving flows driven by accretion disk winds to explain the molecular outflow in F11119+3257 is when we consider the local OH-based momentum outflow rate cited in T15. The X-ray data of T15 strongly suggest that the accretion disk wind is momentum-conserving and being driven by radiation pressure from the AGN. Our data do not allow us to formally rule out the possibility that the much larger OH and CO outflows are also driven by radiation pressure, despite the R^{-2} geometric dilution factor of the AGN radiation field.

It is important to consider the CO and OH outflows together rather than independently. As discussed in Section 4.2, both are likely related to one another but refer to significantly different physical scales ($\sim$0.3 kpc versus 7 kpc) and timescales ($\sim 4 \times 10^5$ yr versus $\sim 7 \times 10^6$ yr). The CO-based momentum outflow rate listed in Table 4 is a quantity that has been time-averaged over a $\sim$100$\times$ longer timescale than the local OH-based momentum outflow rate, so one has to use caution when making direct comparisons between the two molecular outflows and with the present properties of the AGN. Indeed, the CO-based quantities are in much closer agreement with the OH-based quantities that are time-averaged over the flow timescale (R/V). This general agreement between the energetics of the OH and CO outflows suggests that the efficiency of the quasar to drive the large-scale molecular outflow in F11119+3257 has remained relatively constant over the past few $\times$ 10^6 yr. This is not to say that the luminosity of the AGN in F11119+3257 has been constant on shorter timescales (there is evidence that the hard X-ray flux is variable on a timescale of 1 day, although this may be due to variable absorption columns rather than intrinsic variations; T15). Our results simply imply that the quasar has not been dormant for long periods of time over the past few $\times$ 10^6 yr. With this in mind, it is important to use methods that are insensitive to short-term AGN variability when estimating the AGN luminosity. Our use of the global 15–30 μm color (Veilleux et al. 2009) to estimate the fraction of the bolometric luminosity of F11119+3257 produced by the AGN, rather than the (variable) hard X-ray luminosity, mitigates the effects associated with short-term ($\lesssim 10^3$–10^4 yr) AGN variability.

5. Conclusions

We report the results of our analysis of deep new ALMA CO(1−0) data on F11119+3257 obtained in the compact array configuration (∼2.″8 resolution). These data are compared with our findings published in Tombesi et al. (2015) of an X-ray-detected AGN accretion disk wind driving a galaxy-scale energy-conserving molecular (OH) outflow in this object. The main results of this analysis are as follows:

1. The CO(1−0) spectrum shows the presence of broad wings extending $\sim\pm1000\,\mathrm{km\,s^{-1}}$ relative to systemic velocity, indicative of a fast CO outflow with velocities comparable to those measured from the *Herschel* OH 119 μm line profile.
2. Careful photometric and *uv* plane analyses of the ALMA data indicate that the broad-wing CO(1−0) emission extends on a scale of at least ∼7 kpc (radius) from the center. This is the largest molecular outflow found so far in a local ULIRG.
3. The mass of molecular gas involved in the CO outflow is $(0.6\text{–}1.4)\times10^9\,M_\odot$, assuming a ULIRG-like α_{CO} of $0.8\,M_\odot\,(\mathrm{K\,km\,s^{-1}\,pc^2})^{-1}$. This represents ∼7%–20% of the quiescent molecular material in the host galaxy. The flow timescale ($R_{out,CO}/V_{out,CO}$) of this large CO outflow is $\sim7\times10^6$ yr. The molecular mass, momentum, and energy outflow rates time-averaged over the flow timescale are $(80\text{–}200)\,M_\odot\,\mathrm{yr^{-1}}$, $(6\text{–}13)\times10^{35}$ dynes $=(1.5\text{–}3.0)\,L_{AGN}/c$, and $(3\text{–}6)\times10^{43}\,\mathrm{erg\,s^{-1}}=(0.15\text{–}0.40)\%\,L_{AGN}$, respectively ($L_{AGN}=1.5\times10^{46}\,\mathrm{erg\,s^{-1}}$ is the AGN luminosity derived from the infrared 15–30 μm color and the prescription of Veilleux et al. 2009).
4. At face value, the CO-based momentum outflow rate is not inconsistent with the scenario where the CO outflow is momentum conserving and driven by the AGN radiation pressure. This is a different picture than that proposed by Tombesi et al. (2015), who used the local ("instantaneous") value of the OH-based momentum outflow rate estimated at $R\sim300$ pc and valid for timescales $\Delta R_{out,OH}/R_{out,OH}\lesssim10^5$ yr, i.e., nearly two orders of magnitude shorter than the flow timescale of the CO outflow ($\Delta R_{out,OH}$ is the thickness of the outflowing shell of molecular material). In contrast, the OH-based dynamical quantities time-averaged over the flow timescale $R_{out,OH}/V_{out,OH}$ are $R_{out,OH}/\Delta R_{out,OH}=4$ times smaller than the local quantities and thus comparable to the values derived from the CO outflow. These results suggest that the efficiency of the quasar to drive the large-scale molecular outflow in F11119+3257 has remained relatively stable over the past few $\times\,10^6$ yr.

The modest angular resolution of the ALMA data set is a major limitation of our analysis. It will be important to revisit F11119+3257 at higher resolution to constrain the morphology (e.g., distribution and clumpiness) and velocity field of the CO outflow on kiloparsec and subkiloparsec scales. In the long term, F11119+3257 may serve as a local template for future ALMA OH observations in the distant universe, where accretion disk winds are below the detection limits of current X-ray observatories. The launch in the next few years of the *X-Ray Astronomy Recovery Mission*, the replacement for *Hitomi* (*ASTRO-H*), will change the landscape and allow us to search for X-ray winds in the X-ray-brightest ULIRGs with known molecular outflows, as well as some high-redshift quasars. F11119+3257 will be the standard bearer for these future studies.

We thank the anonymous referee for his/her constructive comments, which improved this paper. Partial support from the National Science Foundation through grants AST-1207785 (S.V.), AST-0955836 (A.B.), and AST-1412419 (A.B.) is gratefully acknowledged. S.V. also acknowledges NASA/ADAP grant NNX16AF24G. F.T. acknowledges partial support by NASA through NuSTAR award NNX15AV21G. Basic research in IR astronomy at NRL is funded by the U.S. Office of Naval Research. This paper makes use of the following ALMA data: ADS/JAO.ALMA #2015.1.00305.S. ALMA is a partnership of ESO (representing its member states), NSF (USA), and NINS (Japan), together with NRC (Canada) and NSC and ASIAA (Taiwan), in cooperation with the Republic of Chile. The Joint ALMA Observatory is operated by ESO, AUI/NRAO, and NAOJ. The NRAO is a facility of the National Science Foundation operated under cooperative agreement by Associated Universities, Inc. This work also made use of NASA's Astrophysics Data System Abstract Service and the NASA/IPAC Extragalactic Database (NED), which is operated by the Jet Propulsion Laboratory, California Institute of Technology, under contract with the National Aeronautics and Space Administration.

Facilities: ALMA, *Herschel*, *Suzaku*.

References

Aalto, S., Garcia-Burillo, S., Muller, S., et al. 2012, A&A, 537, A44
Aalto, S., Garcia-Burillo, S., Muller, S., et al. 2015, A&A, 574, A85
Alatalo, K., Blitz, L., Young, L. M., et al. 2011, ApJ, 735, 88
Alatalo, K., Lacy, M., Lanz, L., et al. 2015, ApJ, 798, 31
Arav, N., Borguet, B., Chamberlain, C., Edmonds, D., & Danforth, C. 2013, MNRAS, 436, 3286
Banda-Barragán, W. E., Parkin, E. R., Federrath, C., Crocker, R. M., & Bicknell, G. V. 2016, MNRAS, 455, 1309
Bennett, C. L., Larson, D., Weiland, J. L., & Hinshaw, G. 2014, ApJ, 794, 135
Bolatto, A. D., Warren, S. R., Leroy, A. K., et al. 2013a, Natur, 499, 450
Bolatto, A. D., Wolfire, M., & Leroy, A. K. 2013b, ARA&A, 51, 206
Borguet, B. C. J., Arav, N., Edmonds, D., Chamberlain, C., & Benn, C. 2013, ApJ, 762, 49
Cicone, C., Maiolino, R., Sturm, E., et al. 2014, A&A, 562, A21
Cooper, J. L., Bicknell, G. V., Sutherland, R. S., & Bland-Hawthorn, J. 2009, ApJ, 703, 330
Costa, T., Sijacki, D., & Haehnelt, M. G. 2014, MNRAS, 444, 2355
Evans, A. S., Frayer, D. T., Surace, J. A., & Sanders, D. B. 2001, AJ, 121, 1893
Evans, A. S., Solomon, P. M., Tacconi, L. J., Vavilkin, T., & Downes, D. 2006, AJ, 132, 2398
Fabian, A. C. 2012, ARA&A, 50, 455
Faucher-Giguère, C.-A., & Quataert, E. 2012, MNRAS, 425, 605
Feruglio, C., Fiore, F., Carniani, S., et al. 2015, A&A, 583, 99
Feruglio, C., Maiolino, R., Piconcelli, E., et al. 2010, A&A, 518, L155
Fischer, J., Sturm, E., González-Alfonso, E., et al. 2010, A&A, 518, L41
García-Burillo, S., Combes, F., Usero, A., et al. 2015, A&A, 580, A35
Gaspari, M., & Sadowski, A. 2017, ApJ, 837, 149
González-Alfonso, E., Fischer, J., Graciá-Carpio, J., et al. 2014, A&A, 561, A27
González-Alfonso, E., Fischer, J., Spoon, H., et al. 2017, ApJ, 836, 11
González-Alfonso, E., Fischer, J., Sturm, E., et al. 2015, ApJ, 800, 69
Harrison, C. M., Alexander, D. M., Mullaney, J. R., & Swinbank, A. M. 2014, MNRAS, 441, 3306
Heckman, T. M., Alexandroff, R. M., Borthakur, S., Overzier, R., & Leitherer, C. 2015, ApJ, 809, 147
Kawakatu, N., Imanishi, M., & Nagao, T. 2007, ApJ, 661, 660
Keel, W. C., Chojnowski, S. D., Bennert, V. N., et al. 2012a, MNRAS, 420, 878
Keel, W. C., Lintott, C. J., Maksym, W. P., et al. 2017, ApJ, 835, 256
Keel, W. C., Lintott, C. J., Schawinski, K., et al. 2012b, AJ, 144, 66

Keel, W. C., Maksym, W. P., Bennert, V. N., et al. 2015, AJ, 149, 155
Kim, D.-C., Veilleux, S., & Sanders, D. B. 2002, ApJS, 143, 315
Lindberg, J. E., Aalto, S., Muller, S., et al. 2016, A&A, 587, 15
Maiolino, R., Gallerani, S., Neri, R., et al. 2012, MNRAS, 425, 66
Martí-Vidal, I., Vlemmings, W. H. T., Muller, S., & Casey, S. 2014, A&A, 563, A136
McCourt, M., O'Leary, R. M., Madigan, A.-M., & Quataert, E. 2015, MNRAS, 449, 2
McCourt, M., Oh, S. P., O'Leary, R. M., & Madigan, A.-M. 2016, arXiv:1610.01164
Nardini, E., Reeves, J. N., Gofford, J., et al. 2015, Sci, 347, 860
Nims, J., Quataert, E., & Faucher-Giguère, C.-A. 2015, MNRAS, 447, 3612
Reynolds, C., Punsly, B., Miniutti, G., O'Dea, C. P., & Hurley-Walker, N. 2017, ApJ, 836, 155
Rodríguez Zaurín, J., Tadhunter, C. N., Rose, M., & Holt, J. 2013, MNRAS, 432, 138
Rupke, D. S., Veilleux, S., & Baker, A. J. 2008, ApJ, 674, 172
Rupke, D. S., Veilleux, S., & Sanders, D. B. 2005a, ApJ, 632, 751
Rupke, D. S., Veilleux, S., & Sanders, D. B. 2005b, ApJS, 160, 115
Rupke, D. S. N., & Veilleux, S. 2011, ApJL, 729, L27
Rupke, D. S. N., & Veilleux, S. 2013a, ApJ, 768, 75
Rupke, D. S. N., & Veilleux, S. 2013b, ApJL, 775, L15
Rupke, D. S. N., & Veilleux, S. 2015, ApJ, 801, 126
Scannapieco, E. 2017, ApJ, 837, 28
Scannapieco, E., & Brüggen, M. 2015, ApJ, 805, 158
Schawinski, K., Evans, D. A., Virani, S., et al. 2010, ApJL, 724, L31
Schawinski, K., Koss, M., Berney, S., & Sartori, L. F. 2015, MNRAS, 451, 2517
Scoville, N. Z., Frayer, D. T., Schinnerer, E., & Christopher, M. 2003, ApJL, 585, L105
Solomon, P. M., Downes, D., Radford, S. J. E., & Barrett, J. W. 1997, ApJ, 478, 144
Stern, J., Faucher-Giguère, C.-A., Zakamska, N. L., & Hennawi, J. F. 2016, ApJ, 819, 130
Sturm, E., González-Alfonso, E., Veilleux, S., et al. 2011, ApJL, 733, L16
Tanner, R., Cecil, G., & Heitsch, F. 2016, ApJ, submitted (arXiv:1608.05342)
Thompson, T. A., Fabian, A. C., Quataert, E., & Murray, N. 2015, MNRAS, 449, 147
Thompson, T. A., Quataert, E., Zhang, D., & Weinberg, D. H. 2016, MNRAS, 455, 1830
Tombesi, F., Cappi, M., Reeves, J. N., et al. 2010, A&A, 521, A57
Tombesi, F., Meléndez, M., Veilleux, S., et al. 2015, Natur, 519, 436
Tombesi, F., Tazaki, F., Mushotzky, R. F., et al. 2014, MNRAS, 443, 2154
Turner, B. E., & Gammon, R. H. 1975, ApJ, 198, 71
Veilleux, S., Cecil, G., & Bland-Hawthorn, J. 2005, ARA&A, 43, 769
Veilleux, S., Kim, D.-C., & Sanders, D. B. 2002, ApJS, 143, 315
Veilleux, S., Meléndez, M., Sturm, E., et al. 2013, ApJ, 776, 27
Veilleux, S., Rupke, D. S. N., Kim, D.-C., et al. 2009, ApJS, 182, 628
Walter, F., Bolatto, A. D., Leroy, A. K., et al. 2017, ApJ, 835, 265
Xia, X. Y., Gao, Y., Hao, C.-N., et al. 2012, ApJ, 750, 92
Zubovas, K., & King, A. 2012, ApJL, 745, L34
Zubovas, K., & King, A. 2014, MNRAS, 439, 400